ADVANCED MATERIALS
www.advmat.de

A Suspended, 3D Morphing Sensory System for Robots to Feel and Protect

Wei Zhou, Yi Yu, Peng Xiao, Feng Deng, Yi Zhang, and Tao Chen**

Artificial sensory systems with synergistic touch and pain perception hold substantial promise for environment interaction and human–robot communication. However, the realization of biological skin-like functional integration of sensors with sensitive touch and pain perception still remains a challenge. Here, a concept is proposed of suspended electronic skins enabling 3D deformation-mechanical contact interactions for achieving synergetic ultrasensitive touch and adjustable pain perception. The suspended sensory system can sensitively capture tiny touch stimuli as low as 0.02 Pa and actively perceive pain response with reliable 5200 cycles via 3D deformation and mechanical contact mechanism, respectively. Based on the touch-pain effect, a visualized feedback demo with miniaturized sensor arrays on artificial fingers is rationally designed to give a pain perception mapping on sharp surfaces. Furthermore, the capability is shown of the suspended electronic skin serving as a safe human–robot communication interface from active and passive view through a feedback control system, demonstrating potential in bionic electronics and intelligent robotics.

1. Introduction

Bionic electronic skins (e-skins) have attracted significant interest in emerging fields of wearable electronics,[1] smart prosthetic,[2] soft robots,[3] and human–machine interfaces[4] due to their advantages of high sensitivity, mechanical adaptions, and environment interactions.[5] Among them, flexible tactile sensors with diverse design principles of piezoresistive,[6,7] capacitive,[8,9] piezoelectric,[10,11] triboelectric,[12,13] and iontronic effects[14,15] have been proposed to mimic touch perception. Yet, pain perception is another vital sensation, which can effectively avoid potential dangers and protect themselves.[16,17] Recent researches have shown some typical artificial nociceptors with synaptic-type devices (e.g., transistors or memristors)[18–22] or liquid metal composites.[23] Instead of alternative touch or pain perception, human skin can exhibit the integration of two sensory functions. Therefore, pursuing more intelligent sensory systems with integrated touch and pain perception has drawn more attention in recent years.

Currently, there are two ways to realize integrated sensing for touch and pain. The most typical strategy is to combine force sensors and synaptic-like devices.[24–26] In this case, the output of the force sensors governs the activation of a transistor or a memristor, thereby enabling the dynamic switching between tactile and painful states.[27,28] Another integration strategy is to design single force sensors with unique electrical response behaviors for simultaneous perception of touch and pain. This includes constructing a multilayered electronic dermis with sensitivity differences to distinguish between tactile and nociceptive sensations,[29] as well as developing elastic electronic skins with mutations in sensitivity to realize the transition from touch to pain behaviors.[30] However, both of the above construction strategies present some limitations. Coupling force sensors with artificial synapses in a decentralized deployment would inevitably increase the complexity of the integrated system as well as add to the manufacturing challenges for large-area miniaturized devices. Although the monolithic sensing structures could achieve effective integration, current integrated sensory systems focus on the diverse coupling processes between touch and pain, unable to replicate the sensing performance and functionality of natural biological skin. As depicted in **Figure 1a**, in human skin system, mechanical threshold-induced activation of receptors is responsible for the touch and pain sensations.[31] Moreover, the human skin pursues the perfect integration of ultrasensitive tactile and nociceptive functions, featuring a burst of electrical signals to indicate the dynamic switch between these two senses. Therefore, achieving biological skin-like functional integration of artificial sensory systems with sensitive touch and pain perception through rational material and structure design is full of significance.

W. Zhou, Y. Yu, P. Xiao, F. Deng, Y. Zhang, T. Chen
Key Laboratory of Advanced Marine Materials
Ningbo Institute of Materials Technology and Engineering
Chinese Academy of Sciences
Ningbo 315201, China
E-mail: xiaopeng@nimte.ac.cn; tao.chen@nimte.ac.cn
W. Zhou, Y. Yu, P. Xiao, F. Deng, Y. Zhang, T. Chen
School of Chemical Sciences
University of Chinese Academy of Sciences
19A Yuquan Road, Beijing 100049, China
T. Chen
College of Material Chemistry and Chemical Engineering
Key Laboratory of Organosilicon Chemistry and Material Technology
Ministry of Education
Hangzhou Normal University
Hangzhou, Zhejiang 311121, China

The ORCID identification number(s) for the author(s) of this article can be found under https://doi.org/10.1002/adma.202403447

DOI: 10.1002/adma.202403447

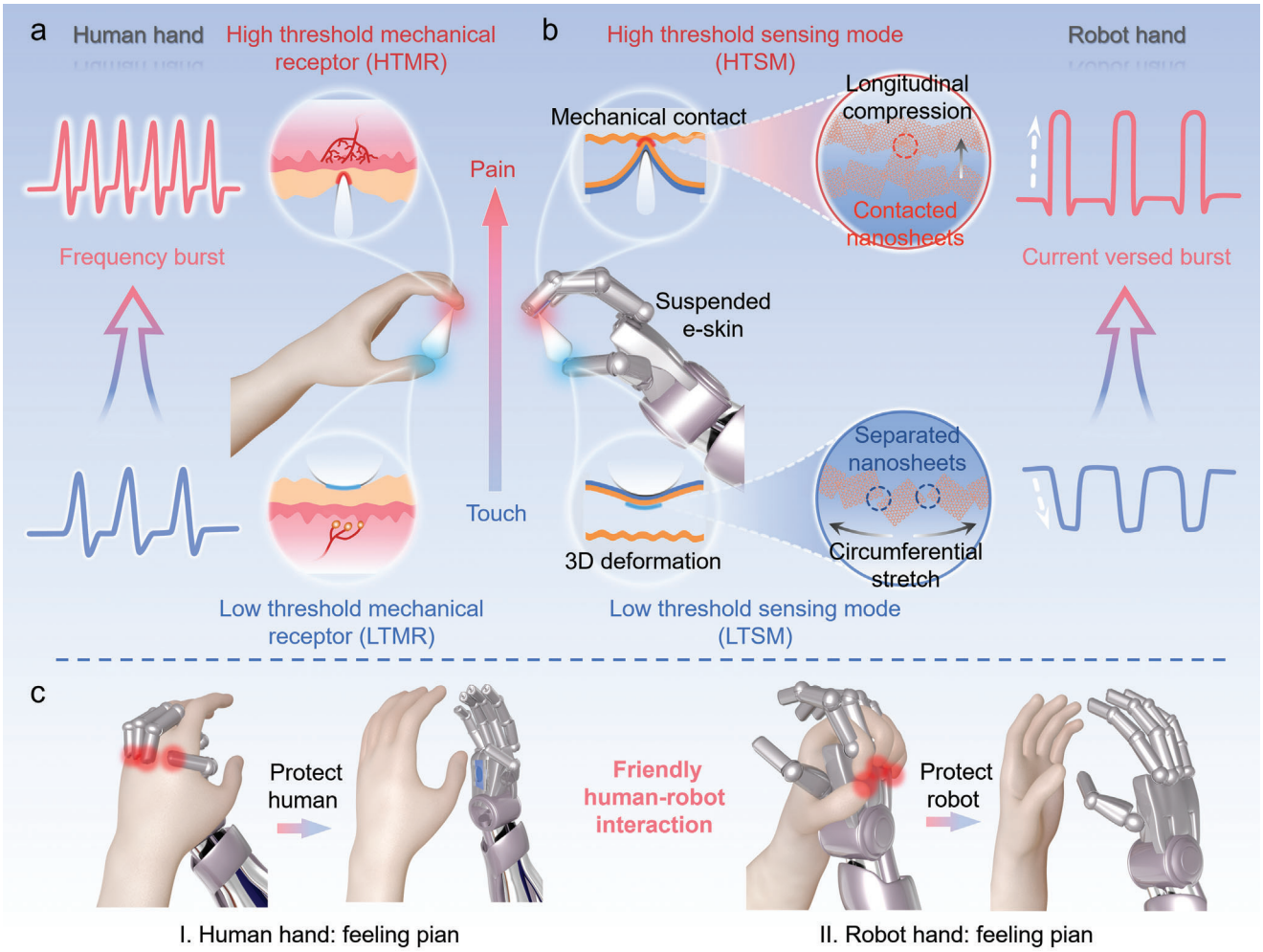

Figure 1. Schematic diagram of bionic suspended sensor with integrated touch and pain sensations. The mechanical threshold-mediated integrated perception of touch and pain for a) human and b) robot hand when touching objects with smooth and sharp surfaces. The bursting behavior of electrical signals indicates the transition from touch to pain in human skin and robotic skin (suspended e-skin), respectively. The circular diagram showing the microscopic deformation mechanisms of graphene nanosheets during touch and pain perception processes. c) The suspended bilayer sensor used as a friendly interface to protect human and robot during human–robot interaction.

Suspended sensing structures play an important role in ultrasensitive tactile sensing due to their excellent deformation capability. However, single suspended structures typically exhibit monotonic electrical output characteristics, failing to achieve the pain response behavior indicated by abrupt electrical signal changes observed in biological skin. Bistable sensing structures mediated by mechanical thresholds have recently attracted widespread research interest. Such structures enable instantaneous configuration reversals upon reaching a mechanical stimulation threshold, eliciting an electrical response featuring abrupt signals.[32,33] Inspired by this, we designed a suspended bilayer sensing structure consisting of graphene sensing film to successfully mimic skin-like mechanical threshold-mediated touch and pain perception. More importantly, the introduced graphene elastic film exhibits 3D deformation and mechanical contact behavior, triggering low-threshold and high-threshold sensing modes (LTSM and HTSM), respectively. At the microscale, graphene nanosheets response to the transition from touch to pain via sequential transverse electrical separation and longitudinal electrical contact, and exhibit current reversal mutation behavior (Figure 1b). Benefiting from the advantage of easy deformation for suspended structures, the as-realized sensor could sensitively capture subtle deformation with the vertical displacement of 20 μm and also detect extremely weak tactile stimulus as low as 0.02 Pa. Moreover, 5200 cycles of electrical contact demonstrate stable pain response behavior without obvious signal drift. As proof of concept, we developed a visualized response system for indicating normal tactile perception and providing early warning of pain based on optical feedback. Furthermore, a miniaturized sensor array was designed and integrated into the dummy fingertips for differentiating the distribution and intensity of touch and pain sensations when in contact with sharp objects. We also demonstrated that the suspended sensor could be used as a friendly interface to protect human and robot during human–robot interaction (Figure 1c). This proposed touch and pain integrated perceptual system with suspended structural design shows great promise towards prosthetic sensory recovery and safe human–machine interactions.

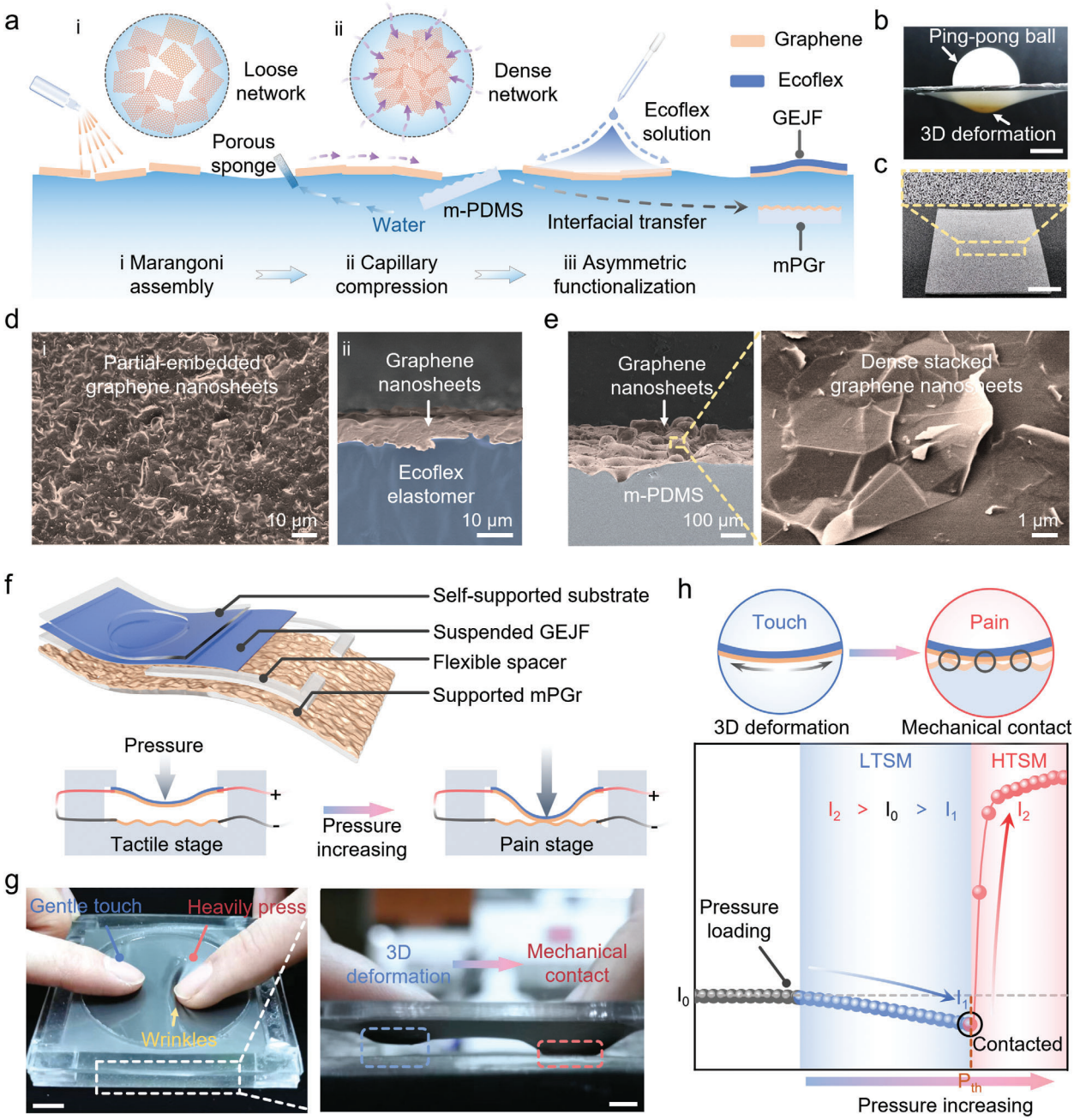

Figure 2. The construction and component of the suspended sensor with integrated touch and pain responses. a) The preparation process of GEJF and mPGr. b) Photo of GEJF in a suspended form exhibiting large deformation under the loading of a ping-pong ball. Scar bar: 2 cm. c) Picture of mPGr with a rough surface, showing distinct metallic luster. Scar bar: 1.5 cm. d) The surface (i) and cross-sectional (ii) SEM images of GEJF with graphene nanosheets partially embedded in Ecofelx matrix. e) The cross-sectional morphology and enlarged image of mPGr. f) The structure of the touch and pain-integrated sensor assembled with suspended and supported conductive layers and the electrode connections as well as the change of contact states at touch and pain stages under pressure loading. g) Photos of a human finger touching the sensor with different levels of pressure, resulting in the suspended elastic film and the supported conductive layer being in separated and contact states, respectively. h) The current response with reverse current mutation and deformation behavior of suspended elastic film in different dimensions, indicating a transition from touch to pain.

2. Results and Discussion

2.1. Fabrication and Characterization of the Suspended e-Skins

The preparation process of the key conductive element in the suspended sensing structure for the integrated touch and pain perception was demonstrated in **Figure** 2a. Here, the graphene nanosheets were selected as the sensing and electrode material due to their excellent conductivity and strain response properties. The modified Langmuir-Blogged (LB) assembly method relying on the water/air active functional platform was adopted for macroscopic assembly of graphene nanosheets.[34–36] This

preparation strategy was chosen mainly for its advantages of a scalable and uniform assembly process, which can serve as an ideal functionalization platform for the controlled fabrication of 2D films. After two sequent approaches including Marangoni-induced preassembly and capillary force driving compression (Figure 2a(i,ii)), a large area of macroscopic graphene film (38 × 43 cm) could be rapidly obtained in a few minutes (Figure S1a, Supporting Information). The SEM image shows the structure of the graphene assembly with densely stacked nanosheets (Figure S2, Supporting Information). Further characterization by Raman spectroscopy demonstrates that the assembled graphene film has fewer lamellar defects (Figure S3, Supporting Information), indicating a substantial advantage of the modified LB method in obtaining high-quality 2D graphene assembly. Afterward, the floated graphene film was further asymmetrically functionalized by Ecoflex to generate elastic graphene/Ecoflex Janus films (GEJF) (Figure S1b, Supporting Information). Further, the obtained GEJF could be easily transferred to a hollow substrate in a suspended form and displayed obvious deformation under the loading of a lightweight ping-pong ball due to its ultrathin and elastic character (Figure 2b). Notably, although conventional fabrication processes based on solid substrates are capable of obtaining ultrathin graphene-based elastic films, it is difficult to achieve efficient and nondestructive transfer as in the case of elastomeric films formed at the water/air interface. Moreover, the asymmetric introduction of Ecoflex endows GEJF with distinct surface morphologies, in which the graphene nanosheets are partially embedded in the Ecoflex matrix to provide excellent conductivity for electrical response (Figure 2d). Meanwhile, because the composite graphene layer is much thinner than Ecoflex matrix, GEJF maintains excellent tensile property and mechanical strength comparable to Ecoflex elastomer (Figure S4, Supporting Information).

Given the excellent transferability of the assembled graphene film at the water/air interface, the obtained graphene film could be composited with microstructured PDMS (m-PDMS) substrate through a direct interfacial transfer approach. The m-PDMS with randomly distributed ridges and pores (Figure S5, Supporting Information) was chosen mainly to increase the adhesion between the graphene film and the substrate (Figure S6, Supporting Information), thus ensuring the stability of the sensing structure and performance under mechanical stimulus. When coated with the conductive graphene film, the surface of m-PDMS/graphene (mPGr) shows a distinct metallic luster (Figure 2c). The cross-sectional SEM of mPGr clearly demonstrates that the microstructure is wrapped by densely connected graphene nanosheets (Figure 2e). More importantly, the surface morphology of mPGr further indicates the continuous distribution of graphene nanosheets even at the location of holes, which would greatly increase the pathway for electron flow to provide outstanding initial electrical conductivity (Figure S7, Supporting Information).

The well-acquired GEJF and mPGr were further laminated face-to-face to form the suspended sensing device. As depicted in Figure 2f, the GEJF was adhered onto a hollow self-supported PDMS substrate as a suspended elastic deformation layer, while the mPGr directly served as the support layer. The upper and lower layers were separated by flexible spacers in advance. It is worth noting that one end of the upper and lower conductive layers was preconnected electrically to enable sequential detection of touch and pain signals in response to increased mechanical stimulus, and the electrodes on the other side were used to connect the test equipment and for voltage input. For such a bilayer sensor with a suspended deformable elastic layer, it could experience tactile and pain responses through different degrees of deformation of the suspended structure with increasing pressure. Moreover, it can simulate the tactile and painful experience of natural biological skin when pressed by a finger. As shown in Figure 2g, the suspended elastic film underwent slight 3D deformation when gently touched by a finger (0.0035 N). As the finger pressed heavily with a force of 1.27 N, the deformation of the elastic film increased and came into contact with the supported layer. It can be clearly observed that irregular wrinkles appear on the surface of the elastic film due to the increase in pressing force and area, similar to the surface state of human skin when subjected to intense pressure. Furthermore, we tested the force variation throughout the finger pressing, the corresponding result indicates that the pressure experiences nonlinear changes from moderate increase to sharp surge (Figure S8, Supporting Information). A pressure threshold (P_{th}) also exists to indicate the transition from touch to pain, which corresponds to the pressure value that triggers the contact between the suspended and supported conductive layers. Moreover, continuous loading enables the nonlinear current output (Figure 2h). In LTSM stage with a noncontact state, the current decreases with increasing pressure, which is caused by the 3D deformation of the suspended elastic film to indicate tactile behavior. When entering the HTSM stage with contact happened, the current increases abruptly in the reverse direction, which is derived from the sufficient electrical contact in the longitudinal direction. It is worth noting that the reversed increased current is first in the pre-pain phase where the current value is less than the initial current, and only when the current exceeds the initial one, it actually enter the pain stage (Figure S9, Supporting Information). Hence, the suspended sensor with 3D deformation-mechanical contact mechanism featuring a reverse current burst allows intuitively distinguishing tactile and painful stimuli, demonstrating unique synergistic perception behavior.

2.2. Study of the Sensing Mechanism

Based on the nonlinear mechanical behavior mediated touch and pain responses, the specific relationship between the current output and pressure input was tested in **Figure 3a**. In the loading process, the pressure increased at an extremely slow rate accompanied by an obvious vertical 3D deformation of the suspended elastic film, leading to a gradual decrease in current (stage-1). When mechanical contact occurred, the increase of pressure accelerated, at which point the current surged in reverse followed by a slow increase immediately (stage-2). As the load was released, the pressure maintaining the contact state fell off instantaneously, resulting in the gradual separation of the elastic film from the underlying conductive layer (stage-3). The corresponding current first decreased slowly and dropped sharply to indicate the disappearance of pain. When the separation process was finished, the 3D deformation of the elastic film gradually recovered due to the slow release of the pressure, allowing the current to

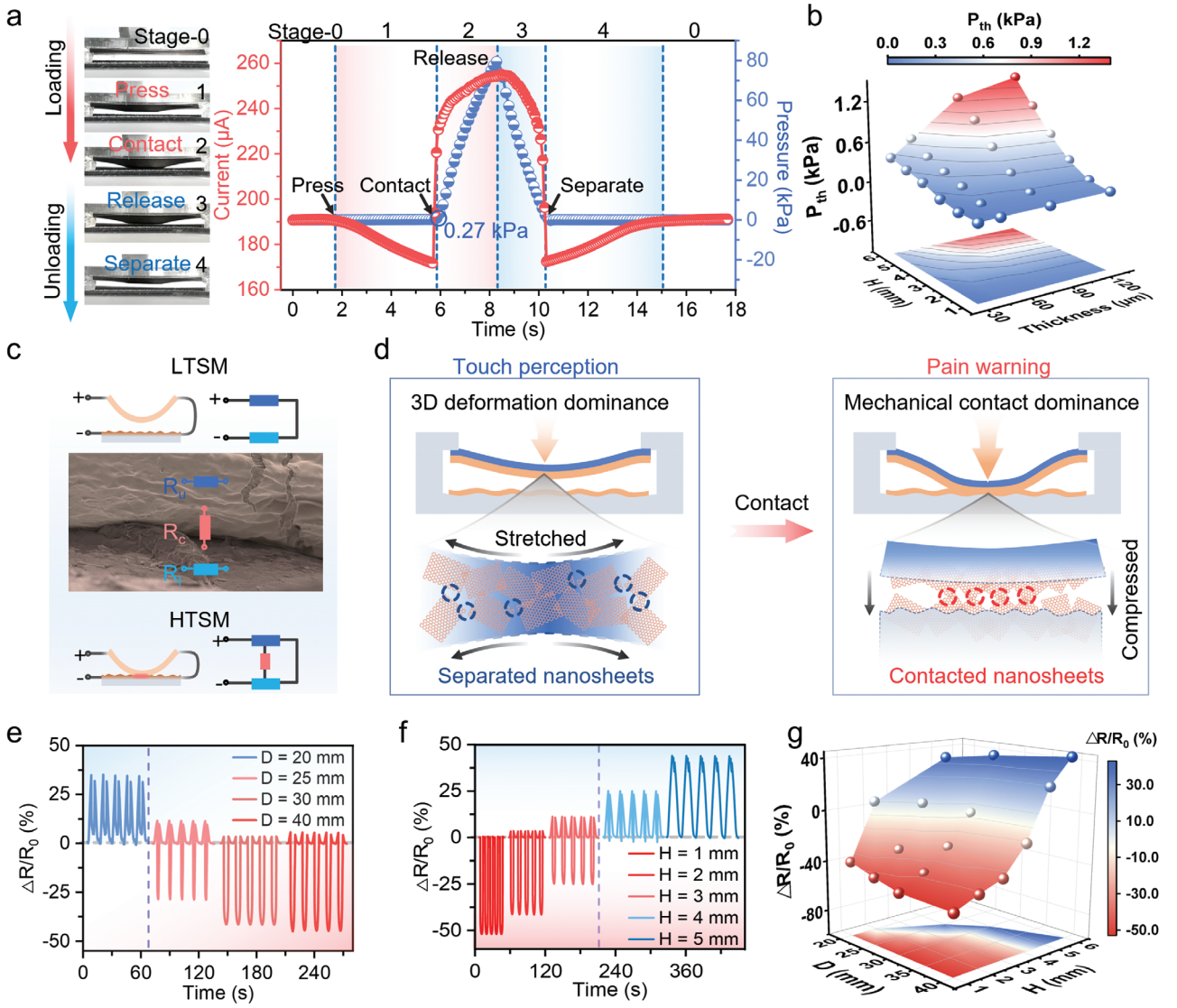

Figure 3. Nonlinear mechanical behavior-induced tactile and pain responses with competing perceptual mechanisms. a) State changes of the upper and lower layers of the suspended sensor during mechanical loading and unloading and the corresponding pressure and current profiles. b) Color mapping of mechanical threshold changes governed by spacer height (*H*) and thickness (*T*) of the suspended elastic film. Data are mean ± s.d. $n = 3$. c) Changes in the resistance connections of the suspended sensor in the LTSM and HTSM stages and the microscopic contact states of the upper and lower layers. d) Schematic of microscopic mechanisms for touch and pain responses. The effect of self-supporting hollow hole diameter e) and spacer height f) on the tactile and pain response performance indicated by the reverse current burst. g) Relative resistance variation with *D* and *H* showing competing touch and pain behaviors. Data are mean ± s.d. $n = 3$.

restore the initial value progressively. Notably, the sensor used here exhibits P_{th} as low as 0.27 kPa, which originates from the inherent feature of easy deformation for the suspended configuration. Moreover, P_{th} could be adjusted by designing the thickness of the suspended elastic film (Figure S10, Supporting Information) and the height of the spacer. As shown in Figure 3b, P_{th} is positively dependent on the thickness and height. This is similar to the nociceptive sensation in biological skin, where the skin with a thicker cortex requires a stronger stimulus to generate pain. Furthermore, the modulation behavior of the suspended film thickness and spacer height on P_{th} was verified by finite element simulations. As shown in Figures S11 and S12, Supporting Information, regardless of thickness or height variations, the suspended film exhibits a two-stage pressure change behavior corresponding to LTSM and HTSM under mechanical stimulation. Further, the simulated stress variations also directly indicate a significant increase in stress after contact due to the low-modulus elastic film compressing the high-modulus substrate, especially at localized microstructural bumps. This also explains the behavior of the sharp pressure increase after mechanical contact. In addition, the theoretical P_{th} was estimated from the simulated pressure profiles, which highly overlapped with the experimental results and increased with the suspended film thickness and the spacer height (Figure S13, Supporting Information). In

particular, changing the spacer height could also give a more pronounced change in P_{th}. Therefore, through choosing the appropriate suspended film thickness and spacer height, the flexible regulation of the pain threshold can be achieved to adapt to diverse application scenarios.

For the mechanical threshold-enabled sensing system, the variation of resistance is directly related to the electrical response in touch and pain stages (Figure 3c). In the LTSM stage, there is a series circuit including the resistance of the upper suspended conductive layer (R_u) and lower supported layer (R_l), in which the change of R_u resulted from the 3D deformation of the suspended elastic film contributes to the current drop behavior for touch perception. Upon contact happens during the HTSM, the contact resistance between the upper and lower conductive layers (R_c) is introduced in a parallel mode. In this case, R_c with a gradual decreasing tendency induced by the continuous increase of pressure is responsible for the reverse increase of current to indicate the pain sensation. The specifical sensing principles for touch and pain are displayed in Figure 3d. In the touch sensing phase, vertical 3D deformation leads to circumferential stretching of the elastomeric film and obvious microcracks observed as displayed in Figure 3c. The embedded graphene nanosheets would move with the elastomer matrix and gradual separate, resulting in the reduction of the conductive pathway. As a result, the current in this stage decreases. When entering the pain stage, the circumferential strain can be ignored and the longitudinal compression dominates, which causes the partially embedded graphene nanosheets at the interface to contact together. Apparently, the electrical contact points gradually increase as the pressure loading, facilitating the flow of electrons along the longitudinal contact interface.

Moreover, the intrinsic nature of this interfacial electrical contact was investigated, where the suspended elastic film was constrained to a glass substrate to exclude the effect of circumferential strain (Figure S14a, Supporting Information). The linear relationship in current–voltage (I–V) curves demonstrates the presence of ohmic contact at the conductive interface (Figure S14b, Supporting Information). Meanwhile, the current output increases with increasing loads, indicating that a good contact state is conducive to electron transport along the contact interface. With such an efficient interfacial electrical contact behavior, it is easy to light up a LED along with enhanced brightness by increasing the interface contact area (Figure S14c, Supporting Information). Moreover, the design of the suspended configuration coupled with the electrical contact behavior could be considered as a general strategy to achieve integrated touch and pain sensations mediated by the 3D deformation-mechanical contact mechanism regardless of which conductive material is chosen (Figure S15, Supporting Information).

However, the pain response behavior is not always present, which is also influenced by the structural parameters, i.e., the height of the spacer (H) and the diameter of the suspended area (D). Specifically, as H increases or D decreases, the reverse increase in current diminishes and even disappears (Figure 3e,f). For example, when D decreases to 20 mm, the sensor ($H = 2$ mm) maintains a positive relative resistance variation of about 4.5% after contact despite the reverse current change, and therefore is only in the pre-pain stage and dose not really perceive pain (Figure 3e). For the sensor with an increase in H to 5 mm, there is no longer a reverse increase in current (Figure 3f). By choosing appropriate structural parameters (D and H), especially by lowering H, the touch and pain response could be perfectly achieved and indicated by the reverse current mutation (Figure 3g). Moreover, the current variation after disconnecting of the initial electrical connection at the contact state was studied in Figure S16a in the Supporting Information. It can be clearly seen that the total current after breaking the electrical connection decreases more and more as H increases. Notably, this reduced part of the current is mainly contributed by the current flowing through the electrical connection. When H is small, the current change resulted from 3D deformation is almost negligible, resulting in a greater tendency for current to pass through the contact interface. As H increases, the current in tactile stage reduces more and more, causing a large proportion of the current to flow through the initial electrical connection rather than the electrical contact interface (Figure S16b, Supporting Information). Therefore, an obvious competition exists between the electrical response in touch and pain stages, in which the resistance variation of the suspended elastic film resulted from the 3D deformation has a significant effect on the pain response behavior after mechanical contact. In Figure S17, Supporting Information, we provide a detailed analysis of the circuit during touch and pain process based on Ohm's law. The contact resistance introduced in parallel after mechanical contact has a dominant role for the pain response, but it is also affected by the resistance of the suspended film at the instant of contact. When the contact resistance is much lower than the resistance of the suspended film, it is more favorable to the behavior of reverse current surge, suggesting an excellent pain response. Therefore, for the sensor designed with a suspended bilayer structure enabling 3D deformation and mechanical contact, the integrated touch and pain perception could be well achieved without the limitation of microscopic conductive materials and macroscopic device size.

2.3. Sensing Performance of the Suspended Bilayer Sensor

The touch and pain sensing performance was investigated in **Figure 4**. For touch stage, the 3D deformation of the suspended elastic film contributes a lot, in which the lateral separation of graphene nanosheets induces an increase in resistance. As shown in Figure 4a, the relative resistance variation displays a positive correlation with the applied pressure and gradually decreases as the enhanced graphene concentration. In general, increasing the concentration leads to a denser stack of graphene nanosheets, which results in an obvious resistance for the nanosheets to slip away. Therefore, the sensor with a low concentration of graphene experiences more disruption of the internal conductive pathway under the same level of pressure stimulation. Also, we calculated the tactile response sensitivity (S) according to the definite equation,[37] $S = (\Delta I/I_0) / \Delta P$. For the suspended elastic film with the graphene concentration of 0.5 mg mL^{-1}, it exhibits a two-stage sensing behavior, with the sensitivity rising from 5.7 to 10.57 kPa^{-1} with pressure loading. Moreover, the thickness of GEJF also affects the tactile sensing performance because the macroscopic deformation of the elastic film is highly dependent on the intrinsic stiffness, which is generally proportional to the thickness. Therefore, the vertical

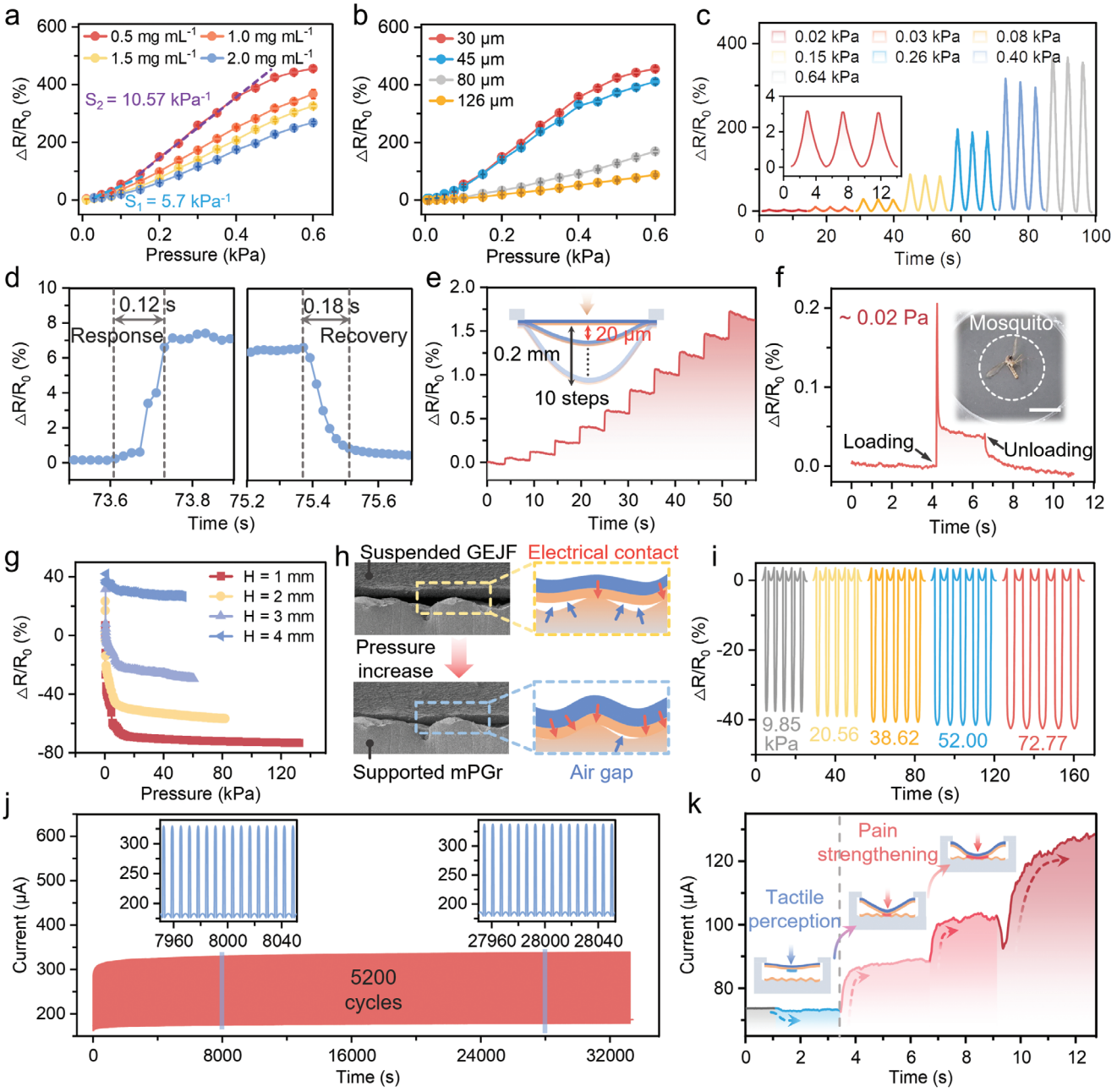

Figure 4. Characterization of tactile and pain response performance. Effect of graphene concentration a) and GEJF thickness b) on touch perception performance. Data are mean ± s.d. $n = 3$. c) Cyclic touch response curves under different pressures. d) Response and recovery time in touch stage. e) Step loading test showing that tiny touch of 20 μm can be distinguished. f) Relative resistance variation of the mosquito load, showing that the suspended sensor has an ultralow limit of touch perception down to 0.02 Pa. The loaded pressure (P) could be calculated by the equation $P = F / S = (mg) / (\pi \times r^2)$, where $m = 1.3$ mg, and r is the radius of the entire suspended area, $r = 1.5$ cm. Inset: Photograph of a lightweight mosquito statically loaded on the surface of a suspended film. Scar bar: 1 cm. g) Changes in nociceptive sensing performance under contact pressure for sensors with different spacers, where the pain level is quantified by the change in relative resistance. h) Changes in microscopic contact states between the upper and lower layers at increasing pressure and the corresponding mechanism diagram. i) Pain cyclic response curves at different contact pressures. j) Pain response performance for 5200 cycles of mechanical contact stimuli at a loading pressure of 50 kPa. k) Real-time changes in current mimicking the touch and pain sensations produced by finger pressing on the human skin.

deformation of the suspended film decreases as the increase of thickness, which in turn endows the sensor with a reduced resistance variation (Figure 4b). Also, the suspended sensor exhibits excellent cyclic responsiveness over a weak pressure range of 0.02–0.64 kPa (Figure 4c). More importantly, the ultralow pressure that cannot be recorded by the commercial force sensor is able to detect by our tactile perceptual system with the vertical displacement down to 50 μm (Figure S18, Supporting Information). In addition, the suspended film could sensitively capture the flow of the air with stable signal output under the airflow

blowing from 0.067 to 8.43 m s^{-1} (Figure S19, Supporting Information), in which the response and recovery time are only 0.12 and 0.18 s for the touch perception (Figure 4d). Based on the feature of easy deformation of the suspended tactile sensing layer, it could even detect the step loads with an interval of only 20 μm in a total deformation of 0.2 mm. As shown in Figure 4e, the suspended sensor could track every tiny deformation synchronously with a stable signal platform. At the same time, a mosquito with ultralight weight of 0.02 Pa could be easily monitored, indicating that the sensor equipped with the suspended configuration has an ultralow detection limit comparable to the reported state-of-the-art works (Figure 4f). The tactile response performance comparison between our graphene-based suspended sensor and other reported important piezoresistive sensors[38–64] was summarized in Figure S20 and Table S1, Supporting Information. Based on the excellent strain response of microscopic 2D graphene nanosheets and the superior deformation capability of macroscopic suspended structures, the elastic suspended tactile system demonstrates an ultralow detection limit along with excellent response sensitivity. In particular, the level of detection limit as low as 0.02 Pa is inaccessible to most pressure sensors reported so far.

When mechanical contact occurs, it indicates the entry into the nociceptive phase. Figure 4g depicts the trend of normalized resistance with contact pressure, suggesting the enhanced pain levels with increasing mechanical pressure, which resulted from the increased electrical contact sites at the interface (Figure 4h). It is worth noting that the pain level varies nonlinearly with pressure, especially at high pressures where the resistance change gradually slows down due to the saturation of contact sites. In addition, the increase in spacer height leads to a prolonged pre-pain phase and a weakened pain response, even causing the pain range to decrease from 132.13 to 60.41 kPa. When $H = 4$ mm, no nociceptive reaction occurs as the resistance change is not reduced to zero, which is mainly attributed to the competing response behaviors between touch and pain stages. As the spacer height increases, the resistance in tactile phase increases more dramatically, resulting in fewer electrons flowing along the electrical contact interface in the pain stage. Pain response curves are demonstrated in Figure 4i, showing favorable cyclic performance with gradual strengthening of the nociceptive response with pressure. Moreover, cyclic stimulus with pressure above the threshold indicates that the suspended sensor possesses a stable pain response without obvious degradation in sensing performance after 5200 cycles of loading, demonstrating superior reliability for long-term use (Figure 4j). Also, we investigated the performance uniformity of the suspended samples obtained from three different sites in the same GEJF. As shown in Figure S21a, Supporting Information, the initial current of the three samples is distributed in a narrow range of 300–500 μA. All three samples exhibit similar tactile and pain sensing performance at different spacer heights (Figure S21b,c, Supporting Information). This demonstrates the clear advantages of the modified LB-based interface assembly strategy in realizing devices with reliable and reproducible electrical and sensing performance.

Based on the outstanding performance of the suspended bilayer sensor in terms of tactile and pain response, a comparison was made with respect to the detection limit and sensing range with the current mainstream piezoresistive pressure sensors[38,39,42–44,47,50,53–56,58,59,64–69] as well as devices with integrated tactile and nociceptive sensing.[27,70] The results in Figure S22 and Table S2, Supporting Information indicate that the suspended electronic skin we developed exhibits both ultralow detection limit (0.02 Pa) and wide sensing range (132.13 kPa), as well as the ability to sense both touch and pain. This is an excellent performance and functional integration that cannot be achieved with currently reported suspended or supported piezoresistive sensors. In particular, the ability to efficiently mimic the synergistic perception of touch and pain in biological skin cannot be achieved based only on a single elastic deformation or mechanical contact-induced resistance changes. By coupling the suspended and supported configuration design and exploiting the sequential 3D deformation and mechanical contact response behavior of the suspended elastic film, our developed sensor achieves efficiently touch and pain integration based on the current mutation response behavior and ensures superior sensing performance for both two stages.

Like the response of biological skin to a continuous tactile and painful stimulus, we mimicked this behavior by applying mechanical stimulus with different loading time, where the plateau corresponding to the maximum resistance change was progressively extended with longer mechanical loading time, suggesting that continuous tactile and nociceptive stimuli were detected (Figure S23, Supporting Information). In addition, we calculated the response/recovery time for the pain stage, which were about 0.2 and 0.85 s, respectively (Figure S24, Supporting Information). This excellent performance was attributed to the microstructures of the PDMS surface that facilitated the rapid contact and detachment between the upper and lower layers. Consequently, the suspended bilayer sensor was able to respond and recover quickly even under prolonged mechanical loading. Compared with the current mainstream piezoresistive sensors,[40,41,44,46–49,52,55–57,65,71–73] the suspended bilayer sensor exhibited good response and recovery performance in both tactile and pain stages (Figure S25, Supporting Information). However, limited by the intrinsic viscoelasticity of the Ecoflex matrix and the adhesion resistance at separation caused by the ultrathin feature of suspended elastic film, current sensor only demonstrated response and recovery speeds on the order of hundred milliseconds. In the future, the development of novel sensing materials and structures that could reduce the interfacial energy dissipation may enable several orders of magnitude improvement (microsecond level) in response and recovery performance.[74]

Finally, we mimicked the touch and pain responses of human skin during finger pressing. As shown in Figure 4k and Figure S26, Supporting Information, a gentle touch simply induced the 3D deformation of the suspended film and indicated the touch perception through a reduced current behavior. When the touch force increased and exceeded the threshold, the current immediately increased in reverse and steadily rose with increasing pressure and pressing area. Further increase in pressure caused an expansion of the compression area, accompanied by a further deformation of the suspended film. As a result, the output current first experienced a transient decrease and then increased in the opposite direction, indicating a pain-strengthening behavior. In brief, the sensor with suspended conductive structures could perfectly indicate touch and pain response behaviors through the phenomenon of current reversal burst, mimicking similar

mechanical threshold-mediated perceptual processes in biological skin.

2.4. Visualization of Touch and Pain Perception

Furthermore, we designed a visualized response system with an integrated light-emitting module to monitor touch information and warn of pain generation, in which two types of signal curves were processed by Arduino and translated into codes similar to 0 and 1 to control the LED to emit blue and red light, respectively (Figure S27a, Supporting Information). The complete circuit includes modules of low-pass filtering, voltage acquisition, data processing, and signal output (Figure S27b, Supporting Information). Among them, the magnitude and slope of the obtained voltage curves corresponding to touch and pain stages were analyzed to guide the corresponding LEDs to emit light. As shown in Figure S28 and Movie S1, Supporting Information, the blue LED turns on during tactile stimulus by blowing in a noncontact way or by direct contact with a pen tip equipped with a hard EVA block. As pressure increases and triggers mechanical contact, the red LED immediately turns on along with a distinct reverse mutation of voltage, indicating a painful warning. Notably, the pain signal tends to experience a momentary tactile response before the reversed mutation, thus the blue LED flashes briefly before the red LED lights up, which also demonstrates the fast responsiveness of the visualized intelligent touch and pain feedback system.

Also, we explored the effect of the objects' sharpness on the tactile and pain response. As shown in Figure S29a, Supporting Information, three objects with different sharpness levels were designed and investigated corresponding mechanical behavior in the process of stimulating the suspended sensor. The result in Figure S29b (Supporting Information) indicates that the suspended film in contact with the sharpest surface would experience a more pronounced 3D deformation and contact with the lower layer earliest for pain response. The summarized pain threshold in Figure S29c (Supporting Information) also shows the lowest pain threshold for the sensor touching object 1. Therefore, it is not difficult to conclude that the sharper the surface of the object, the more likely it is to cause pain feeling to the suspended e-skin under the same level of pressure stimulation. Based on this special response behavior, we interconnected the suspended sensor and LEDs modules and assembled them on an artificial hand to realize visual tactile and pain feedback from touching objects with varying sharpness (**Figure 5**a). In general, human palms are more likely to produce pain when touching rough surfaces. This is because rough surfaces cause more pronounced deformation of the skin at the same level of touch strength, which activates pain receptors (Figure 5b). Coincidentally, the suspended sensor has similar touch and pain sensations when touching smooth and rough surfaces (Figure 5c). As shown in Figure 5c and Figure S30, Supporting Information, when the artificial hand equipped with suspended sensor gently touches both smooth and rough surfaces ($F < F_R$), the suspended elastic film immediately deforms, and more pronounced deformation occurred upon contact with rough surfaces. As the touching force increases ($F_s < F < F_R$), the red LED corresponding to the rough surface is illuminated to warn of pain generation. In contrast, the sensor that touches the smooth surface simply increases the deformation degree without contacting the underlying conductive layer, thus keeping the blue LED lit. The exact operation was illustrated in Figure 5d and Movie S2, Supporting Information. It can be clearly seen that as the touch force increases, the red LED in the visualized sensing system for touching a rough stone tends to light up, warning of potential danger. The corresponding voltage profile is shown in Figure 5d, where touching the smooth stone simply produces upward increasing voltage signals to represent the tactile information, whereas touching the rough stone produces a significant reverse voltage change with the increase of pressure, thus indicating the generation of pain.

Based on the excellent size designability of this suspended sensor, we further designed miniaturized sensors with a lateral dimension of 1*1 cm and attached them to the fingertips of an artificial hand for touch and pain detection (Figure 5f). Among them, the self-supporting substrate was replaced by 200-μm thick PET with a hollow diameter of 5 mm, and the spacer height was reduced to 200 μm. With such a rational design, the artificial hand could be used to detect the touch and pain distribution at the fingertips when touching a durian shell. As shown in Figure 5g, the fingers touching the spines on the surface of the durian shell all show varying degrees of pain response, while the thumb touching the smooth edge of the durian indicates a touch state (Figure S31, Supporting Information). In addition, the optical feedback-based visualized system is also introduced into the sensor array, in which the red LED lights up when the index finger touches the sharp durian shell to warn of pain generation (Figure 5h).

2.5. Suspended e-Skin for Friendly Human–Robot Interaction

Based on the outstanding performance of the suspended sensor with the integrated functions of normal tactile sensing and injury pain warning, it could be used as the "skin" of the robot to realize the construction of a friendly human–robot interaction system (**Figure 6**a). Here, the well-defined interactive system consists of signal acquisition, signal processing, and signal output modules (Figure 6b). Among them, the microcontroller in the signal processing module acts like the brain of the robot, allowing a deep analysis of the acquired voltage signals. The well-analyzed signal is then transmitted to the control component of the robot hand to perform the intended actions. The principle of the specific action execution is displayed in Figure S32 in the Supporting Information. For the collected voltage signal in tactile stage, the amplitude of the voltage change (ΔV) and the corresponding threshold (ΔV_{th}) is mainly analyzed and compared. If ΔV is greater than ΔV_{th}, the tactile action would be executed. Similarly, for the pain signal, the corresponding action is performed when the change slope of reverse voltage (S) is smaller than the threshold (S_{th}). We first remotely controlled the action execution with touch and pain responses. As shown in Figure S33a and Movie S3, Supporting Information, when the sensor was lightly touched, the robot hand made a victory gesture corresponding to our predefined tactile action. When pressing hard and causing mechanical contact behavior, the robot hand quickly performed a predefined fist-clenching action. Moreover, the robotic hand responds quickly with a stable output of two-stage signals under multiple cycles of tactile and pain stimuli (Figure S33b, Supporting Information), demonstrating its reliability for practical applications.

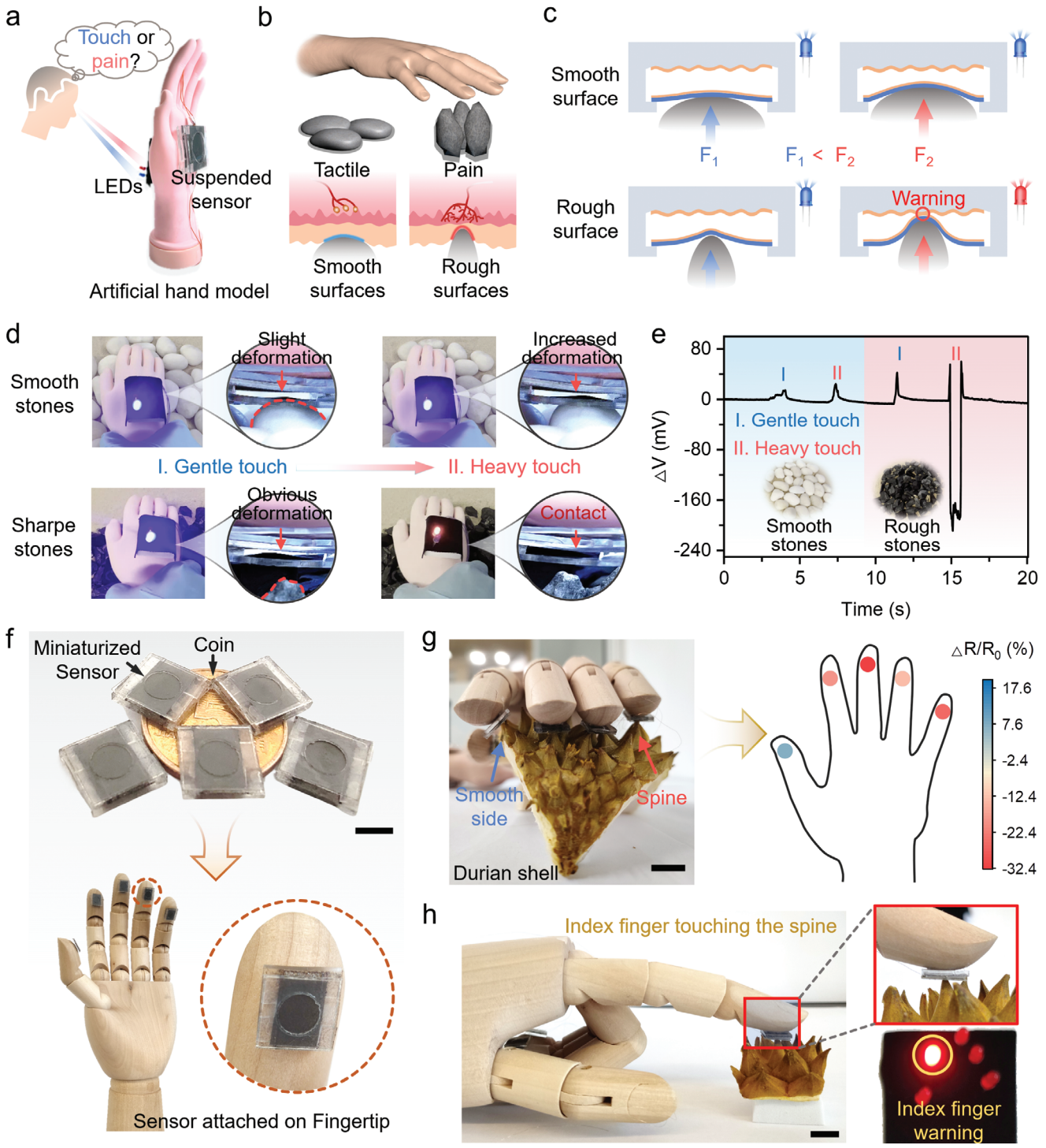

Figure 5. Visualized touch and pain intelligent response system. a–e) Visualized tactile and pain state indication with an artificial hand touching smooth and rough surfaces. a) Artificial hand with integrated suspended sensor and LED module is used to provide immediate touch and pain stimulus information based on optical feedback. b) Schematic of tactile and pain perceptual behavior of a human hand in touching smooth and rough surfaces. c) Diagram of the principle for visualized tactile and pain responses of the suspended sensor when touching smooth and rough surfaces with increasing pressure. d) The contact states of the suspended sensor and the luminescence of the LEDs when touching the smooth and rough surfaces, where the increase in pressure results in the red LED lighting up when touching the rough stone surface, indicating the generation of pain. e) The output voltage curves when the artificial hand touching the smooth and rough stones with varying pressures. f–h) Touch and pain perception of the miniaturized sensor array. f) Photo of the miniaturized sensors distributed on and around a coin and further attached to the fingertips of a dummy hand. Scar bar: 0.5 cm. g) Photograph of a dummy hand touching a durian shell, showing the thumb touching the smooth edge and the other four fingers touching the spines. The right is the color mapping of touch and pain responses on the five fingers. h) Photo of the index finger touching the spine on the durian shell and the red LED in the corresponding position lit to indicate the production of pain.

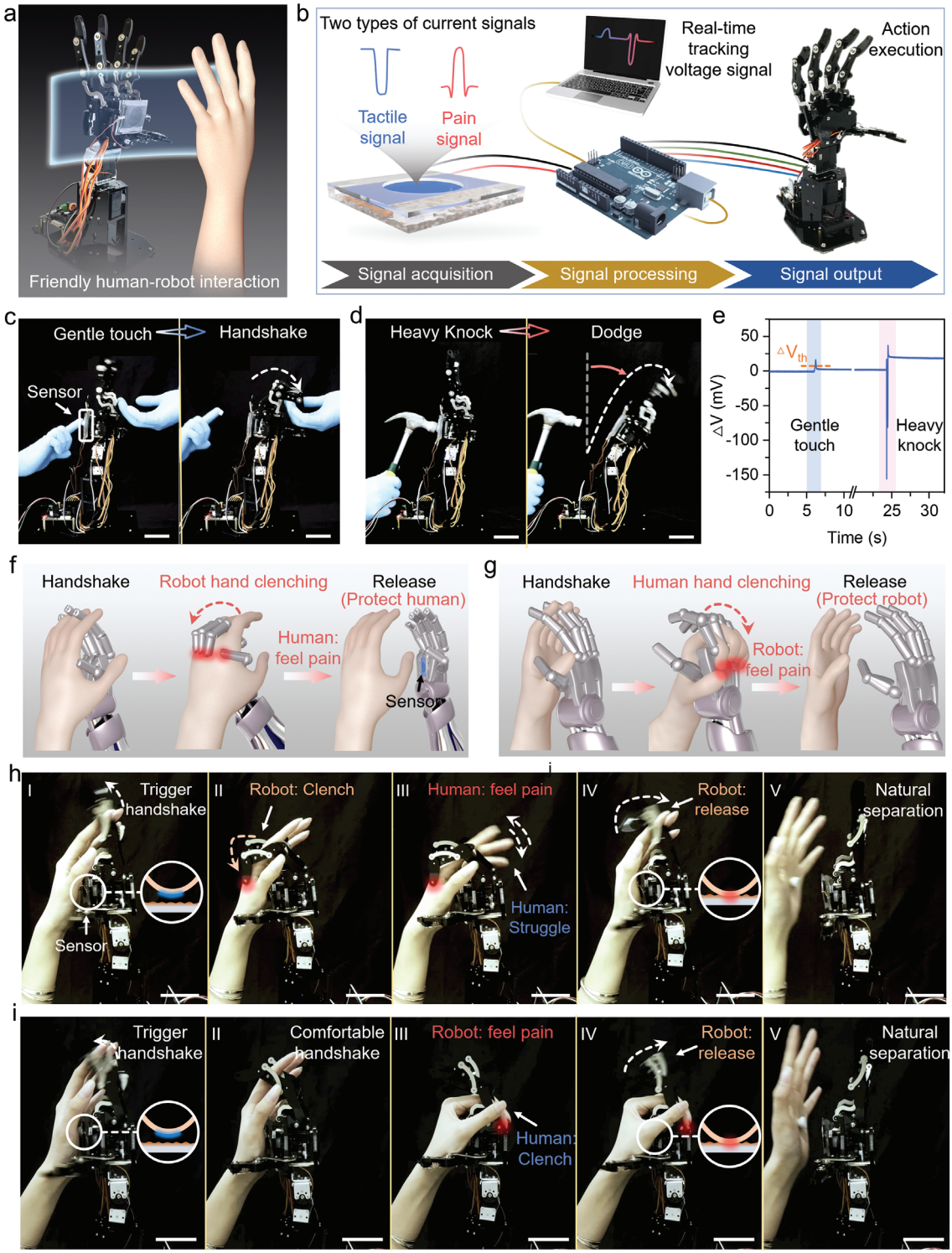

Figure 6. Touch and pain-integrated sensor for friendly human–robot interaction. a) Schematic representation of the suspended sensor integrated into the robot hand as a safe communication interface to facilitate friendly human–robot interaction. b) Composition of the friendly human–robot interaction system. c–e) The sensor attached to the back of the robot hand is used as a self-aware interface for autonomous control of the robot hand. c) The robot hand detects tactile signals and triggers a handshake action. Scar bar: 5 cm. d) The robot hand senses the painful information of a hammer strike and performs a forward flip action to dodge the danger. Scar bar: 5 cm. e) The voltage signals corresponding to these two processes in (c) and (d). f–i) The touch and pain integrated sensor is used as a friendly human–robot interface to achieve active protection for the robot and human during interaction. f) Schematic and h) experimental pictures of the robot clenching the human hand to make it feel pain and achieving protection to human by actively releasing its hand. Scar bar: 5 cm. g) Diagram and i) experimental photos of a human hand clenching a robot hand to make it feel pain and protecting it by actively releasing the hand of the robot. Scar bar: 5 cm.

Notably, it is difficult to achieve continuous operation in two mechanical stimuli because of the time it takes for the robot hand to execute the movement and for the control system to acquire the initial voltage signal. However, benefiting from the good responsiveness of the suspended bilayer sensors, the robot hand was able to respond rapidly following the applied mechanical stimulus without obvious delay. The fast and reliable response allows us to further attach the sensor to the back of the robotic hand to be used as a self-aware protection interface (Movie S4, Supporting Information). Here, the robotic hand automatically detects and responds to different levels of mechanical stimulus. For example, when the human hand gently touched the sensor at the back, the robotic hand would sense the touch signal and actively shake hands in a predetermined manner (Figure 6c). However, when a hammer struck the sensor heavily, the robot hand immediately turned the palm forward to dodge the danger and protect itself (Figure 6d). The corresponding voltage curve is shown in Figure 6e, in which the rising voltage signal implies the detected tactile response, and the set action is triggered when the change value exceeds the threshold. For the sharp drop in voltage signal caused by a hard hit, the robotic hand immediately recognizes it as pain information and initiates the avoidance action for protection. Hence, by detecting and processing touch and pain signals, the robotic hand can achieve perfect self-awareness and self-protection.

During human–robot interaction, it is necessary to ensure the safety of the human on the one hand and to protect the robot skin on the other hand. Here, by integrating the sensor into the robot palm, effective protection of both the robot and the human can be achieved. As shown in Figure 6f,g, when a human and a robot shake hands, inappropriate force control may result in pain sensation for the human or robot hand. With this integrated touch and pain-sensing interface, it is possible for the robot to perceive pain from its own or the human, and further actively release hand to avoid injury. The first case is shown in Figure 6h and Movie S5, Supporting Information, where a handshake is triggered when the human hand gently touches the suspended sensor (Figure 6h(I)). At this point, there is a voltage variation above the threshold in the monitored signal curve (Figure S34a, Supporting Information). As the robot hand continues handshake and holds it too tightly, the human hand will feel pain and try to struggle (Figure 6h(II)). Once the violent struggle of the human hand leads to contact between the upper and lower conductive layers, the robot would immediately sense the discomfort of the human hand and actively release the hand to protect it from further injury (Figure 6h(III–V)). Notably, in order to avoid the shaking of the human hand to transmit interference signals, we have preset that tactile action is considered to be over and the pain behavior is performed immediately only when the reverse mutation of the voltage signal is detected. In the second case in Movie S6, Supporting Information, the robot and human are initially in a relatively comfortable handshake (Figure 6i(I)). However, when the human hand suddenly tightens its grip and touches the lower conductive layer of the sensor, the robot feels pain and immediately performs a release action (Figure 6i(II–IV)). Accordingly, the human releases the hand, providing effective and timely protection for the robot (Figure 6i(V)). The ascending voltage signal in Figure S34b (Supporting Information) corresponds to the triggering of the handshake action, while the reverse sharp decrease in the voltage indicates the generation of pain to control the release of the robot hand. Hence, a friendly human–robot interaction could be efficiently achieved through such a suspended sensing interface with integrated perception of touch and pain.

3. Conclusion

We have presented a integrated touch and pain sensory system mediated by suspended electronic skins with dynamic 3D deformation and mechanical contact interactions, enabling the robot hand to actively recognize mechanical pain and react for self-protection and protecting human beings. Different from the conventional multi-devices coupling principle enabled touch and pain system, our proposed sensor is highly structurally integrated with suspended and supported elastic conductive films for high-sensitive touch sensation and pain alarming indicated by the reverse mutation behavior of the current. The suspended configuration allows for sensitive capture of subtle deformation, capable of resolving tiny dynamic displacements of 20 μm and detecting extremely weak tactile information as low as 0.02 Pa. Moreover, stable and reliable pain response is demonstrated with 5200 cycles of mechanical contact, showing great advantages of long-term operation in practical application.

To further elevate the performance of a single sensory device, a closed-loop control system is integrated to realize real-time mechanical stimuli capture, recognition, feedback, and final reaction. As a demo, a visualized response system coupled with optical feedback module is proposed to indicate touch and pain states. Also, we show that a well-designed miniaturized sensor array can act as wearable finger sensory system that can give a 2D mapping of different levels of touch and pain sensation upon the sharp objects. More importantly, we demonstrate that the commercial robot hand-sensor integrated system can function as an efficient and safe human–robot interaction interface, which can actively protect human beings from machine injury and also avoid the unfavorable injury from mechanical force.

However, there is still room for further improvement. First, the pain threshold of the suspended structure is much lower than the actual level of human skin. For real human skin, the statistically obtained pain threshold is around 500 kPa by means of a pressurization test combined with the quantification of the Wong–Baker face pain rating and the numerical pain rating.[75,76] Increasing the deformation resistance of the suspended film via designing an elastic suspended layer with mechanical strain stiffening effect[77] or the introduction of filling medium between the two layers may contribute to the enhanced pain threshold. Besides, the present pain perception function does not have the similar allodynia behavior of human body, i.e., after producing pain, it will lower the threshold of pain perception and thus show pain to normal stimuli.[26] In our system, the height of the spacer between the two layers plays an important role in the pain threshold. Therefore, the alternative dielectric elastomers[78] could be considered to act as flexible and dynamically adjustable spacers, enabling the achievement of adaptive threshold modulation for skin-like allodynia behavior. Finally, in order to improve the sensing accuracy and area of suspended bilayer sensors, it is necessary to construct large-area sensor arrays by massively integrating miniaturized sensors. In this regard, the introduction of an automated manufacturing process contributes to the consistency of

sensor performance. In addition, the crosstalk between the sensing pixels will highly affect the spatial resolution. Further design and optimization of sensing structures and circuits to achieve crosstalk resistance is necessary. Notably, the increase in array density also limits the information processing capability. By introducing advanced algorithms (machine learning and deep learning, etc.)[79] and adopting a distributed information processing model,[80] the information processing efficacy in large-area sensor array will be greatly improved. In a word, proceeding with the optimization of material/device structures and updating of software/hardware systems, we anticipate that the suspended bilayer sensory system based on the 3D deformation and mechanical contact mechanism shows great promise for applications in bionic electronics and smart human–robot interactions.

Supporting Information

Supporting Information is available from the Wiley Online Library or from the author.

Acknowledgements

W.Z. and Y.Y. contributed equally to this work. This work was supported by the National Key Research and Development Program of China (2022YFC2805200), Natural Science Foundation of China (52373094, 52073295), Sino-German Mobility Program (M-0424), Ningbo International Cooperation (2023H019). The authors also thank Prof. Patrick Théato from the Karlsruhe Institute of Technology for his thoughtful suggestions.

Conflict of Interest

The authors declare no conflict of interest.

Data Availability Statement

The data that support the findings of this study are available from the corresponding author upon reasonable request.

Keywords

3D deformation, friendly human–robot interface, mechanical contact, suspended e-skin, tactile and pain perception

Received: March 7, 2024
Revised: April 22, 2024
Published online:

[1] S. Li, H. Wang, W. Ma, L. Qiu, K. Xia, Y. Zhang, H. Lu, M. Zhu, X. Liang, X.-E. Wu, H. Liang, Y. Zhang, *Sci. Adv.* **2023**, *9*, eadh0615.
[2] A. Chortos, J. Liu, Z. Bao, *Nat. Mater.* **2016**, *15*, 937.
[3] J. Shi, Y. Dai, Y. Cheng, S. Xie, G. Li, Y. Liu, J. Wang, R. Zhang, N. Bai, M. Cai, Y. Zhang, Y. Zhan, Z. Zhang, C. Yu, C. F. Guo, *Sci. Adv.* **2023**, *9*, eadf8831.
[4] X. Cai, Y. Xiao, B. Zhang, Y. Yang, J. Wang, H. Chen, G. Shen, *Adv. Funct. Mater.* **2023**, *33*, 2304456.
[5] W. Zhou, P. Xiao, T. Chen, *Acc. Mater. Res.* **2023**, *4*, 334.
[6] M. Cai, Z. Jiao, S. Nie, C. Wang, J. Zou, J. Song, *Sci. Adv.* **2021**, *7*, eabl8313.
[7] Q. Wei, G. Chen, H. Pan, Z. Ye, C. Au, C. Chen, X. Zhao, Y. Zhou, X. Xiao, H. Tai, Y. Jiang, G. Xie, Y. Su, J. Chen, *Small Methods* **2022**, *6*, 2101051.
[8] N. Bai, L. Wang, Y. Xue, Y. Wang, X. Hou, G. Li, Y. Zhang, M. Cai, L. Zhao, F. Guan, X. Wei, C. F. Guo, *ACS Nano* **2022**, *16*, 4338.
[9] C. Lv, C. Tian, J. Jiang, Y. Dang, Y. Liu, X. Duan, Q. Li, X. Chen, M. Xie, *Adv. Sci.* **2023**, *10*, 2206807.
[10] W. Lin, B. Wang, G. Peng, Y. Shan, H. Hu, Z. Yang, *Adv. Sci.* **2021**, *8*, 2002817.
[11] J. Zhang, H. Yao, J. Mo, S. Chen, Y. Xie, S. Ma, R. Chen, T. Luo, W. Ling, L. Qin, Z. Wang, W. Zhou, *Nat. Commun.* **2022**, *13*, 5076.
[12] X. Qu, Z. Liu, P. Tan, C. Wang, Y. Liu, H. Feng, D. Luo, Z. Li, Z. L. Wang, *Sci. Adv.* **2022**, *8*, eabq2521.
[13] D. Lu, T. Liu, X. Meng, B. Luo, J. Yuan, Y. Liu, S. Zhang, C. Cai, C. Gao, J. Wang, S. Wang, S. Nie, *Adv. Mater.* **2023**, *35*, 2209117.
[14] P. Lu, L. Wang, P. Zhu, J. Huang, Y. Wang, N. Bai, Y. Wang, G. Li, J. Yang, K. Xie, J. Zhang, B. Yu, Y. Dai, C. F. Guo, *Sci. Bull.* **2021**, *66*, 1091.
[15] Q. Liu, Z. Liu, C. Li, K. Xie, P. Zhu, B. Shao, J. Zhang, J. Yang, J. Zhang, Q. Wang, C. F. Guo, *Adv. Sci.* **2020**, *7*, 2000348.
[16] Y. Zhang, Y. Fang, J. Li, Q. Zhou, Y. Xiao, K. Zhang, B. Luo, J. Zhou, B. Hu, *ACS Appl. Mater. Interfaces* **2017**, *9*, 37493.
[17] A. E. Dubin, A. Patapoutian, *J. Clin. Invest.* **2010**, *120*, 3760.
[18] G. Feng, J. Jiang, Y. Zhao, S. Wang, B. Liu, K. Yin, D. Niu, X. Li, Y. Chen, H. Duan, J. Yang, J. He, Y. Gao, Q. Wan, *Adv. Mater.* **2020**, *32*, 1906171.
[19] J. Ge, S. Zhang, Z. Liu, Z. Xie, S. Pan, *Nanoscale* **2019**, *11*, 6591.
[20] Y. Kim, Y. J. Kwon, D. E. Kwon, K. J. Yoon, J. H. Yoon, S. Yoo, H. J. Kim, T. H. Park, J.-W. Han, K. M. Kim, C. S. Hwang, *Adv. Mater.* **2018**, *30*, 1704320.
[21] M. Xiao, D. Shen, M. H. Futscher, B. Ehrler, K. P. Musselman, W. W. Duley, Y. N. Zhou, *Adv. Electron. Mater.* **2020**, *6*, 1900595.
[22] R. A. John, N. Tiwari, M. I. B. Patdillah, M. R. Kulkarni, N. Tiwari, J. Basu, S. K. Bose, C. J. Yu, A. Nirmal, S. K. Vishwanath, C. Bartolozzi, A. Basu, N. Mathews, *Nat. Commun.* **2020**, *11*, 4030.
[23] E. J. Markvicka, R. Tutika, M. D. Bartlett, C. Majidi, *Adv. Funct. Mater.* **2019**, *29*, 1900160.
[24] M.d. A. Rahman, S. Walia, S. Naznee, M. Taha, S. Nirantar, F. Rahman, M. Bhaskaran, S. Sriram, *Adv. Intell. Syst.* **2020**, *2*, 2000094.
[25] R. Yu, Y. Yan, E. Li, X. Wu, X. Zhang, J. Chen, Y. Hu, H. Chen, T. Guo, *Mater. Horiz.* **2021**, *8*, 2797.
[26] F. Li, S. Gao, Y. Lu, W. Asghar, J. Cao, C. Hu, H. Yang, Y. Wu, S. Li, J. Shang, M. Liao, Y. Liu, R.-W. Li, *Adv. Sci.* **2021**, *8*, 2004208.
[27] F. Yu, J. C. Cai, L. Q. Zhu, M. Sheikhi, Y. H. Zeng, W. Guo, Z. Y. Ren, H. Xiao, J. C. Ye, C.-H. Lin, A. B. Wong, T. Wu, *ACS Appl. Mater. Interfaces* **2020**, *12*, 26258.
[28] Y. Sun, Y. Dong, Z. Li, Q. Li, M. Liu, Q. Yuan, B. Li, *Chem. Eng. J.* **2024**, *482*, 148945.
[29] L. E. Osborn, A. Dragomir, J. L. Betthauser, C. L. Hunt, H. H. Nguyen, R. R. Kaliki, N. V. Thakor, *Sci. Robot.* **2018**, *3*, eaat3818.
[30] P. Xiao, W. Zhou, Y. Liang, S.-W. Kuo, Q. Yang, T. Chen, *Adv. Funct. Mater.* **2022**, *32*, 2201812.
[31] V. E. Abraira, D. D. Ginty, *Neuron* **2013**, *79*, 618.
[32] H. L. Ferrand, A. R. Studart, A. F. Arrieta, *ACS Nano* **2019**, *13*, 4752.
[33] K. S. Riley, S. Koner, J. C. Osorio, Y. Yu, H. Morgan, J. P. Udani, S. A. Sarles, A. F. Arrieta, *Adv. Intell. Syst.* **2022**, *4*, 2200158.
[34] W. Zhou, P. Xiao, C. Zhang, Q. Yang, T. Chen, *Mater. Horiz.* **2023**, *10*, 1264.
[35] W. Zhou, P. Xiao, Y. Liang, Q. Wang, D. Liu, Q. Yang, J. Chen, Y. Nie, S.-W. Kuo, T. Chen, *Adv. Funct. Mater.* **2021**, *31*, 2105323.
[36] S. Wang, Y. Gao, A. Wei, P. Xiao, Y. Liang, W. Lu, C. Chen, C. Zhang, G. Yang, H. Yao, T. Chen, *Nat. Commun.* **2020**, *11*, 4359.
[37] R. Chen, T. Luo, J. Wang, R. Wang, C. Zhang, Y. Xie, L. Qin, H. Yao, W. Zhou, *Nat. Commun.* **2023**, *14*, 6641.

[38] Z. Xu, D. Wu, Z. Chen, Z. Wang, C. Cao, X. Shao, G. Zhou, S. Zhang, L. Wang, D. Sun, *Microsyst. Nanoeng.* **2023**, *9*, 5.
[39] N. Li, S. Gao, Y. Li, J. Liu, W. Song, G. Shen, *Nano Res.* **2023**, *16*, 7583.
[40] Y. Hou, L. Wang, R. Sun, Y. Zhang, M. Gu, Y. Zhu, Y. Tong, X. Liu, Z. Wang, J. Xia, Y. Hu, L. Wei, C. Yang, M. Chen, *ACS Nano* **2022**, *16*, 8358.
[41] J. Xu, H. Li, Y. Yin, X. Li, J. Cao, H. Feng, W. Bao, H. Tan, F. Xiao, G. Zhu, *npj Flex. Electron.* **2022**, *6*, 62.
[42] J. Suo, Y. Liu, C. Wu, M. Chen, Q. Huang, Y. Liu, K. Yao, Y. Chen, Q. Pan, X. Chang, A. Y. L. Leung, H. Chan, G. Zhang, Z. Yang, W. Daoud, X. Li, V. A. L. Roy, J. Shen, X. Yu, J. Wang, W. J. Li, *Adv. Sci.* **2022**, *9*, 2203565.
[43] K. Cao, M. Wu, J. Bai, Z. Wen, J. Zhang, T. Wang, M. Peng, T. Liu, Z. Jia, Z. Liang, L. Jiang, *Adv. Funct. Mater.* **2022**, *32*, 2202360.
[44] D. Geng, S. Chen, R. Chen, Y. You, C. Xiao, C. Bai, T. Luo, W. Zhou, *Adv. Mater. Technol.* **2022**, *7*, 2101031.
[45] W. Li, X. Jin, X. Han, Y. Li, W. Wang, T. Lin, Z. Zhu, *ACS Appl. Mater. Interfaces* **2021**, *13*, 19211.
[46] Y. M. Yin, H. Y. Li, J. Xu, C. Zhang, F. Liang, X. Li, Y. Jiang, J. W. Cao, H. F. Feng, J. N. Mao, L. Qin, Y. F. Kang, G. Zhu, *ACS Appl. Mater. Interfaces* **2021**, *13*, 10388.
[47] X. Wang, L. Tao, M. Yuan, Z. Wang, J. Yu, D. Xie, F. Luo, X. Chen, C. Wong, *Nat. Commun.* **2021**, *12*, 1776.
[48] Y.-R. Kim, M. P. Kim, J. Park, Y. Lee, S. K. Ghosh, J. Kim, D. Kang, H. Ko, *ACS Appl. Mater. Interfaces* **2020**, *12*, 58403.
[49] Y. Cheng, Y. Ma, L. Li, M. Zhu, Y. Yue, W. Liu, L. Wang, S. Jia, C. Li, T. Qi, J. Wang, Y. Gao, *ACS Nano* **2020**, *14*, 2145.
[50] J. Wang, C. Zhang, D. Chen, M. Sun, N. Liang, Q. Cheng, Y. Ji, H. Gao, Z. Guo, Y. Li, D. Sun, Q. Li, H. Liu, *ACS Appl. Mater. Interfaces* **2020**, *12*, 51854.
[51] D. Wang, L. Wang, Z. Lou, Y. Zheng, K. Wang, L. Zhao, W. Han, K. Jiang, G. Shen, *Nano Energy* **2020**, *78*, 105252.
[52] T. Zhao, T. Li, L. Chen, L. Yuan, X. Li, J. Zhang, *ACS Appl. Mater. Interfaces* **2019**, *11*, 29466.
[53] S. Chun, W. Son, H. Kim, S. K. Lim, C. Pang, C. Choi, *Nano Lett.* **2019**, *19*, 3305.
[54] M. Wang, Y. Qiu, J. Jia, C. Wang, J. Deng, K. Pan, *Adv. Mater. Technol.* **2019**, *4*, 1800363.
[55] Z. Han, Z. Cheng, Y. Chen, B. Li, Z. Liang, H. Li, Y. Ma, X. Feng, *Nanoscale* **2019**, *11*, 5942.
[56] B. Yin, X. Liu, H. Gao, T. Fu, J. Yao, *Nat. Commun.* **2018**, *9*, 5161.
[57] Z. Wang, S. Guo, H. Li, B. Wang, Y. Sun, Z. Xu, X. Chen, K. Wu, X. Zhang, F. Xing, L. Li, W. Hu, *Adv. Mater.* **2019**, *31*, 1805630.
[58] Y. Pang, K. Zhang, Z. Yang, S. Jiang, Z. Ju, Y. Li, X. Wang, D. Wang, M. Jian, Y. Zhang, R. Liang, H. Tian, Y. Yang, T.-L. Ren, *ACS Nano* **2018**, *12*, 2346.
[59] K. Xia, C. Wang, M. Jian, Q. Wang, Y. Zhang, *Nano Res.* **2018**, *11*, 1124.
[60] Y. Gao, H. Ota, E. W. Schaler, K. Chen, A. Zhao, W. Gao, H. M. Fahad, Y. Leng, A. Zheng, F. Xiong, C. Zhang, L.-C. Tai, P. Zhao, R. S. Fearing, A. Javey, *Adv. Mater.* **2017**, *29*, 1701985.
[61] M. Liu, X. Pu, C. Jiang, T. Liu, X. Huang, L. Chen, C. Du, J. Sun, W. Hu, Z. L. Wang, *Adv. Mater.* **2017**, *29*, 1703700.
[62] M. Jian, K. Xia, Q. Wang, Z. Yin, H. Wang, C. Wang, H. Xie, M. Zhang, Y. Zhang, *Adv. Funct. Mater.* **2017**, *27*, 1606066.
[63] S. Gong, W. Schwalb, Y. Wang, Y. Chen, Y. Tang, J. Si, B. Shirinzadeh, W. Cheng, *Nat. Commun.* **2014**, *5*, 3132.
[64] H. Yao, J. Ge, C. Wang, X. Wang, W. Hu, Z. Zheng, Y. Ni, S. Yu, *Adv. Mater.* **2013**, *25*, 6692.
[65] X. Wei, H. Li, W. Yue, S. Gao, Z. Chen, Y. Li, G. Shen, *Matter* **2022**, *5*, 1481.
[66] M. Zhong, L. Zhang, X. Liu, Y. Zhou, M. Zhang, Y. Wang, L. Yang, D. Wei, *Chem. Eng. J.* **2021**, *412*, 128649.
[67] Y. W. Choi, D. Kang, P. V. Pikhitsa, T. Lee, S. M. Kim, G. Lee, D. Tahk, M. Choi, *Sci. Rep.* **2017**, *7*, 40116.
[68] J. Park, M. Kim, Y. Lee, H. S. Lee, H. Ko, *Sci. Adv.* **2015**, *1*, 1500661.
[69] Y. Li, Y. Wei, Y. Yang, L. Zheng, L. Luo, J. Gao, H. Jiang, J. Song, M. Xu, X. Wang, W. Huang, *Research* **2022**, *2022*, 0002.
[70] Q. Xia, Y. Qin, P. Qiu, A. Zheng, X. Zhang, *J. Mater. Chem. B* **2022**, *10*, 1991.
[71] Z. Chen, Y. Hu, H. Zhuo, L. Liu, S. Jing, L. Zhong, X. Peng, R. Sun, *Chem. Mater.* **2019**, *31*, 3301.
[72] Y. Zhang, Q. Lu, J. He, Z. Huo, R. Zhou, X. Han, M. Jia, C. Pan, Z. L. Wang, J. Zhai, *Nat. Commun.* **2023**, *14*, 1252.
[73] Y. Ma, Y. Yue, H. Zhang, F. Cheng, W. Zhao, J. Rao, S. Luo, J. Wang, X. Jiang, Z. Liu, N. Liu, Y. Gao, *ACS Nano* **2018**, *12*, 3209.
[74] Y. Zhang, X. Zhou, N. Zhang, J. Zhu, N. Bai, X. Hou, T. Sun, G. Li, L. Zhao, Y. Chen, L. Wang, C. F. Guo, *Nat. Commun.* **2024**, *15*, 3048.
[75] G. Park, C. W. Kim, S. B. Park, M. J. Kim, S. H. Jang, *Ann. Rehabil. Med.* **2011**, *35*, 412.
[76] D. Han, M. Park, J. Choi, H. Shin, D. Kim, S. Rhim, *Sens. (Basel Switz.)* **2022**, *22*, 2996.
[77] M. Vatankhah-Varnosfaderani, A. N. Keith, Y. Cong, H. Liang, M. Rosenthal, M. Sztucki, C. Clair, S. Magonov, D. A. Ivanov, A. V. Dobrynin, S. S. Sheiko, *Science* **2018**, *359*, 1509.
[78] H. Zhao, A. M. Hussain, M. Duduta, D. M. Vogt, R. J. Wood, D. R. Clarke, *Adv. Funct. Mater.* **2018**, *28*, 1804328.
[79] Y. Wang, M. L. Adam, Y. Zhao, W. Zheng, L. Gao, Z. Yin, H. Zhao, *Nano Micro Lett.* **2023**, *15*, 55.
[80] J. Lee, K. Cho, J. Kim, *Adv. Mater.* **2024**, *36*, 2310505.